

# Direct Observation of Modulated Radical Spin States in Metal–Organic Frameworks by Controlled Flexibility

Xiaofeng Chen,<sup>\*,†,‡,#</sup> Haomiao Xie,<sup>‡,#</sup> Emmaline R. Lorenzo,<sup>‡</sup> Charles J. Zeman,<sup>‡</sup> Yue Qi,<sup>‡</sup> Zoha H. Syed,<sup>‡</sup> Aaron E.B.S. Stone,<sup>‡</sup> Yao Wang,<sup>§</sup> Subhadip Goswami,<sup>‡</sup> Peng Li,<sup>§</sup> Timur Islamoglu,<sup>‡</sup> Emily A. Weiss,<sup>‡</sup> Joseph T. Hupp,<sup>‡</sup> George C. Schatz,<sup>‡</sup> Michael R. Wasielewski,<sup>‡</sup> and Omar K. Farha<sup>\*,‡</sup>

<sup>†</sup>School of Environmental and Geographical Sciences, Shanghai Normal University, Shanghai 200234, China.

<sup>‡</sup>Department of Chemistry, Northwestern University, Evanston, Illinois 60208, United States.

<sup>§</sup> Shanghai Key Laboratory of Molecular Catalysis and Innovative Materials, Department of Chemistry, Fudan University, Shanghai 200438, China.

---

**ABSTRACT:** Owing to their switchable spin states and dynamic electronic character, organic-based radical species have been invoked in phenomena unique to a variety of fields, such as biology, materials development, chemistry, and physics. When incorporated in solid state materials, generation of organic radicals proves challenging due to aggregation. Metal-organic frameworks (MOFs) are promising candidates for immobilization and stabilization of organic radicals because of the tunable spatial arrangement of organic linkers and metal nodes, which sequesters the reactive species. Herein, a flexible, redox-active tetracarboxylic acid linker bearing two imidazole units was chosen to construct a new Zr<sub>6</sub>-MOF, **NU-910**, with *scu* topology. By exploiting the structural flexibility of **NU-910**, we, for the first time, successfully modulate the dynamics between an isolated organic radical species and an organic radical  $\pi$ -dimer species. Single-crystal X-ray diffraction (SCXRD) analysis reveals that through solvent exchange from N, N-diethylformamide to acetone, **NU-910** undergoes a structural contraction with interlinker distances decreasing from 8.32 Å to 3.20 Å at 100 K. Organic radical species on the bridging linkers are generated via UV light irradiation. Direct observation of temperature-induced spin switches from an isolated radical species to a magnetically silent radical  $\pi$ -dimer in **NU-910** was achieved *via* variable temperature single-crystal X-ray diffraction and variable temperature electron paramagnetic resonance (EPR) spectroscopy of **NU-910** after irradiation in the solid state. Ultraviolet-Visible-Near Infrared (UV-vis-NIR) Spectroscopy and Density Functional Theory (DFT) calculations further substantiated the formation of a radical cation  $\pi$ -dimer upon irradiation. This work demonstrates the potential of using flexible MOFs as a platform to modulate radical spin states in the solid phase.

---

## INTRODUCTION

Upon application of an external stimulus, such as pressure, temperature, guest molecules and/or light, certain chemical species can undergo a spin state switch—this proves useful for applications involving molecular electronics and spintronics because of the accessibility of switchable bistable states at the molecular level.<sup>1–6</sup> The change of spin state in a molecule not only induces a change in molecular magnetic moment but also triggers changes in molecular connectivity and optical properties due to the resultant altering of electronic structure and/or formation of covalent/secondary bonds.<sup>7,8</sup> The most well-known systems for these purposes are organometallic complexes with spin crossover properties.<sup>9–11</sup> In these species, the spin states of the metal center can transition between high-spin and low-spin states following interaction with the aforementioned external stimuli.<sup>2,12,13</sup> In the past few decades, spin switches based on organic radicals have attracted attention. This is due to

their desirable features, such as rich structural diversity and the multitude of synthetic tools and methods available for their construction.<sup>14–19</sup> Nevertheless, despite the numerous varieties of radicals (including spin switches) that are observed in solution-phase systems, isolation of radicals in the solid state has proven to be quite nontrivial due to rapid dimerization, which can form either  $\sigma$ -dimers or multicentered  $\pi$ -dimers.<sup>20</sup> Furthermore, organizing these organic radicals in the solid state with preserved switchability of spin states still remains challenging.<sup>19,21,22</sup>

Metal-organic frameworks (MOFs) are a type of porous material comprised of metal-containing nodes and organic linkers.<sup>23,24</sup> As a scaffold, functional moieties can be installed onto the highly ordered framework at the metal nodes and/or organic linkers.<sup>25–28</sup> Moreover, different molecular arrangements in the solid state can be achieved by carefully choosing metal nodes and organic linkers with suitable geometries.<sup>29–31</sup> Beyond the chemical functionali-

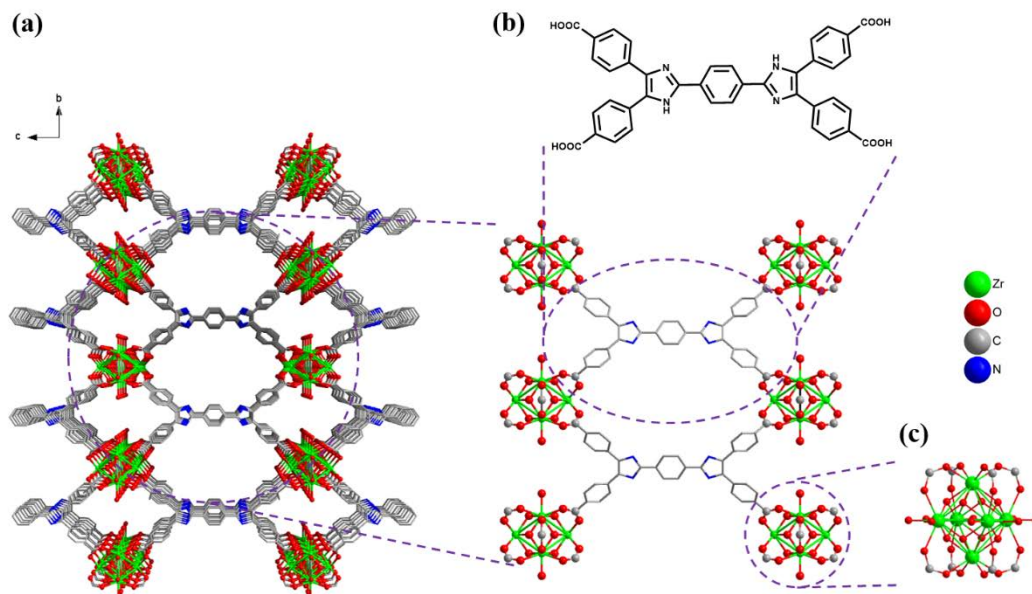


**Figure 1.** Relevant structural features and representations of **NU-910**. (a) Structure of **NU-910** (view from a-axis) (b) Structure of **H<sub>4</sub>BBI** linker and (c) 8-connected **Zr<sub>6</sub>** cluster. All hydrogen atoms are omitted for clarity.

ties that define a MOF, physical behaviors such as “breathing” (i.e., expansion and contraction of the unit cell) have also been encountered.<sup>32-35</sup> To this end, a MOF can undergo structural transformability between an “open pore” (*op*) configuration and a “closed pore” (*cp*) configuration triggered by external stimuli.<sup>32, 36, 37</sup> From *op* to *cp*, interlinker distances can be altered significantly; this is a testament to the flexibility a MOF can often exhibit even with rigid connectivity. For example, MOFs featuring hexazirconium (IV) clusters as metal nodes have been extensively investigated due to their excellent thermal and chemical stability from the strong Zr-O bonds.<sup>38, 39</sup> However, the **Zr<sub>6</sub>** node usually induces structural rigidity owing to the high connectivity. In this case, incorporation of flexible linkers is a straightforward way to introduce flexibility to **Zr<sub>6</sub>**-MOFs.<sup>40, 41</sup> The topology of MOFs also plays an important role in flexibility. For instance, between the two most common MOF topologies (*scu* and *csq*) with tetracarboxylic acid-based linkers, *scu* is more frequently used for flexible MOFs since the interconnected mesopore and micropore in *csq* topology can further rigidify the MOF skeleton to a certain extent.<sup>42-45</sup>

Keeping this reticular chemistry in mind, we envisioned flexible MOFs as a promising platform for regulating the dynamics between a paramagnetic isolated radical species and a diamagnetic radical  $\pi$ -dimer species. Such is accomplished by adjusting the distance between two adjacent linkers. From a characterization standpoint, the crystalline nature of MOFs enables direct observation of the structural changes in functional moieties by single-crystal X-ray diffraction (SCXRD) analysis, which provides deeper insights into the structure-property relationship upon irradiation.

Introduction of redox-active organic linkers such as viologens,<sup>46-48</sup> naphthalene diimides,<sup>49-51</sup> tetrathiafulvalene<sup>52, 53</sup> into MOFs have been applied to stabilize organic radicals. Specifically, tetrathiafulvalene was incorporated into the

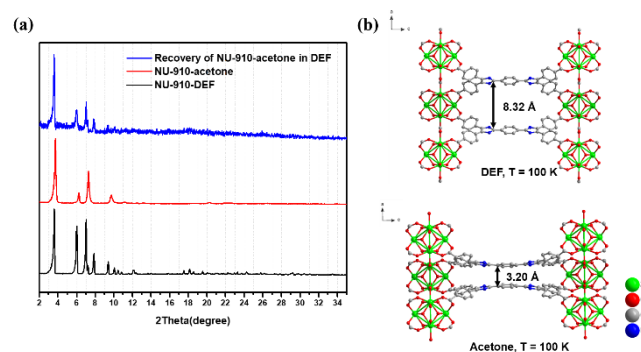


**Figure 2.** (a) PXRD patterns of **NU-910-DEF**, **NU-910-acetone**, and the recovery of **NU-910-acetone** from **DEF**. (b) interlinker distances of **NU-910-DEF** and **NU-910-acetone** at 100K. All hydrogen atoms are omitted for clarity.

skeleton of MOFs to modulate the breathing behavior through redox reactions that accompanied the structural changes of ligands.<sup>54</sup> Although numerous MOFs with redox-active linkers for generation of radicals have been reported, utilizing the flexibility of MOFs to modulate radical spin states in the solid state is less precedented. To test the efficacy of MOF flexibility as a vehicle for modulation of radical spin, a flexible tetracarboxylic acid linker bearing two imidazole units, 4,4',4'',4'''-(1,4-phenylenebis(1H-imidazole-2,4,5-triyl))tetrabenzoic acid,<sup>55</sup> (**H<sub>4</sub>BBI**, Figure 1), was synthesized to construct a new **Zr<sub>6</sub>**-MOF, **NU-910**, with *scu* topology.

## RESULTS AND DISCUSSION

**Structure Analysis.** Yellow rod-shaped single crystals of **NU-910** were obtained by solvothermal synthesis using benzoic acid and acetic acid as modulators in *N,N*-diethylformamide (DEF) overnight in the oven at 120 °C (see the Supporting Information, pg. S2). The structure of **NU-910**

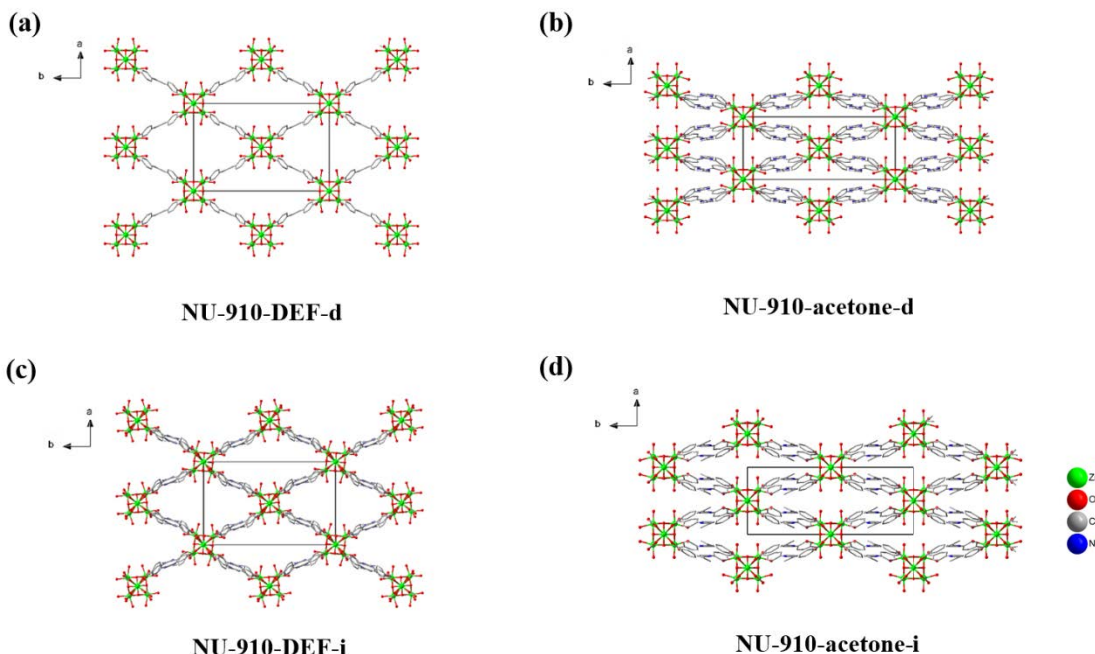


**Figure 3.** Crystal structures of **NU-910-DEF** (a, c) and **NU-910-acetone** (b, d) before and after irradiation at 100 K. Grey rectangle represents unit cell. All hydrogen atoms are omitted for clarity.

was revealed by single-crystal X-ray diffraction at 100 K. **NU-910** crystallized in the *Cmmm* space group as  $[\text{Zr}_6(\mu\text{-O})_4(\mu\text{-OH})_4(\text{C}_6\text{H}_5\text{COO})_x(\text{OOCCH}_3)_{4-x}(\text{BBI})_2]_z$ . The 8-connected Zr<sub>6</sub> cluster sits at the *D*<sub>2h</sub> symmetry site and is connected by eight tetratopic carboxylate linkers, **BBI**<sup>4-</sup>, with *C*<sub>2h</sub> symmetry and is identified as the (4,8)-*c scu* topology (Figure 1). The structure has diamond-shaped channels along *a*-axis (with a diameter ~ 6 Å) connected by small windows in *c* direction. Interestingly, we found that the **NU-910** showed reversible structural flexibility in different solvents. The PXRD of **NU-910** changes dramatically after the solvent exchange from DEF to acetone, namely **NU-910-DEF** and **NU-910-acetone**, respectively, and the structure in acetone could be converted back to that in DEF after being immersed in DEF overnight (Figure 2a). The SCXRD results show that the unit cell changes dramatically from *Cmmm* (*a*= 16.6375(3) Å, *b*= 25.7093(4) Å, *c*= 24.5828(3) Å) in DEF to *Cmmm* (*a*= 11.2882(4) Å, *b*= 27.3986(5) Å, *c*= 24.3982(5) Å) in acetone. After solvent exchange from DEF to acetone, the rhombic framework stretched along the *a*-axis and shortened along the *b* axis while leaving the *c* direction almost unchanged with a 33% reduction of unit cell volume from 10515 Å<sup>3</sup> to 7549 Å<sup>3</sup> (Figure 3a, b). A closer inspection of the SCXRD structure in acetone reveals that the **BBI** linker has a static disorder at two distinct positions. Instead of being planar, a distortion bending along the *a*-axis is found in the **NU-910-acetone** structure either upward or downward with 0.5/0.5 occupancy. A close *π-π* stacking between two adjacent **BBI** linkers is observed with around 3.20 Å interlinker distance, which is much shorter than 8.32 Å in the phase from **NU-910-DEF** (Figure 2b). As a result, instead of having interconnected pores, one-dimensional channels

with 7 Å diameter are found in **NU-910-acetone**. This is consistent with the Density Functional Theory (DFT)-calculated pore size distribution obtained from N<sub>2</sub> sorption at 77 K (Figure S1). Notably, the C-C bond distance between the phenyl ring and imidazole rings is 1.43(2) Å in **NU-910-acetone**, which is comparable to that in **NU-910-DEF** (1.467(8) Å), indicating that the oxidation state of **BBI** linkers remains unchanged during the structural contraction in the dark.

Bridged imidazole dimers are known to generate radical species upon UV irradiation.<sup>56-58</sup> Indeed, **H<sub>4</sub>BBI** also shows a signal at *g* = 2.000, (Figure S2a) in the electron paramagnetic resonance (EPR) spectrum after irradiation, indicating the generation of a radical species. The radical generation properties of **NU-910-acetone** were also investigated. As depicted in Figure S2b, **NU-910-acetone** showed a signal indicative of a radical species. The signal with *g<sub>z</sub>* = 2.026, *g<sub>y</sub>* = 2.007 and *g<sub>x</sub>* = 2.000 is ascribed to superoxide ions on the Zr<sub>6</sub> nodes instead of organic radical.<sup>59, 60</sup> Visually, **NU-910** underwent a color change from yellow to dark green when exposed to UV light, while **H<sub>4</sub>BBI** didn't show an obvious color change after irradiation (Figure S3). The green photoactivated sample slowly returned to the initial color overnight when placed in the dark, which substantiates that the photochromic processes are qualitatively reversible. This behavior corresponded well to the decay of EPR signals over time (Figure S4). The PXRD patterns of **NU-910-acetone** and **NU-910-DEF** showed only a slight shift of peaks to higher angles after irradiation, which correlates well with the simulated PXRD pattern from the collected SCXRD data (Figure S5). The **BBI**<sup>4-</sup> linker in **NU-910-acetone** and **NU-910-DEF** remained stable after irradiation,

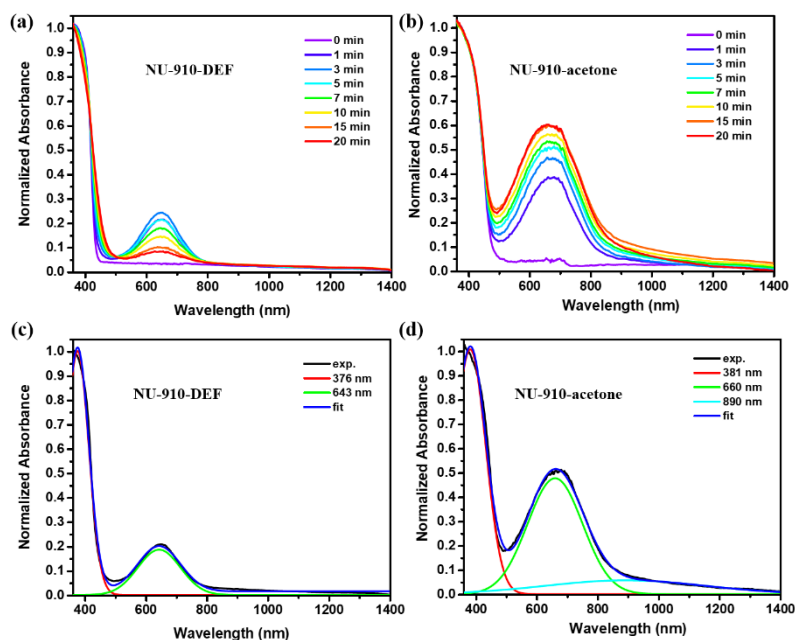


**Figure 4.** Time-dependent UV-vis-NIR absorption spectra of **NU-910-DEF** (a, c) and **NU-910-acetone** (b,d) under irradiation at room temperature ( $\lambda = 390$  nm).

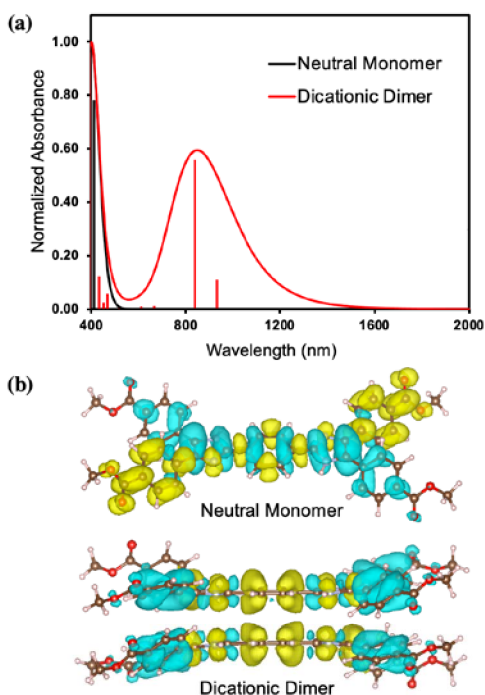


**Figure 5.** Calculated absorption spectra (a) and charge-difference densities (b) of a charge-neutral monomer corresponding to the 412 nm transition and a dicationic dimer of **BBI** corresponding to the 839 nm transition using B3LYP-D3 with implicit solvent.

which was further confirmed by  $^1\text{H}$  Nuclear Magnetic Resonance (NMR) spectroscopy (Figure S6, S7). These results demonstrate that the observed photochromism is not from photolysis or structural transformation.

**Absorption Spectral Study.** To uncover the origin of the color change after irradiation, Ultraviolet-Visible-Near Infrared (UV-Vis-NIR) spectroscopy was employed. As shown in Figure 4, the unirradiated **NU-910**, **NU-910-DEF-d** ( $d = \text{in the dark}$ ) and **NU-910-acetone-d**, displayed absorption bands below 500 nm, due to the  $n-\pi^*$  and  $\pi-\pi^*$  transitions of the **BBI**<sup>4+</sup> linker. Under UV irradiation, only trivial changes were observed for the linker (Figure S8), while an intense well-defined new absorption band from 500 nm to 1400 nm was observed for **NU-910-acetone-i** (Figure 4b,  $i = \text{irradiated}$ ). The intensity gradually increased with the duration of irradiation. Combined with the EPR signal, we ascribed the new absorption peak to the organic radical species on the linker. Furthermore, this broad absorption band can be deconvoluted into two peaks, one centered at 660 nm and the other at 890 nm (Figure 4d). In contrast, **NU-910-DEF-i** showed a much narrower absorption peak from 500 nm to 800 nm after irradiation (Figure 4a). This corresponded to the first peak of **NU-910-acetone**, though the peak at 890 nm is absent (Figure 4c). The intensity of the new peak from the organic radical for **NU-910-DEF-i** is also weaker compared to that of **NU-910-acetone-i**, due to a possible quenching effect from DEF solvent.<sup>54</sup> The spectral difference between **NU-910-acetone-i** (*cp* structure) and **NU-910-DEF-i** (*op* structure) implies the new peak in the NIR region for **NU-910-acetone-i** is induced by the short distance between the **BBI** linkers, and could be derived from the formation of a radical  $\pi$ -dimer.

**DFT Calculations.** To elucidate the nature of the transitions observed in Figure 4, DFT was used. Following methods adapted from the literature,<sup>61</sup> excitation spectra were calculated for a variety of possible charge combinations on the isolated monomer and the dimer of an ester-functionalized **BBI** linker. It was found that a dicationic **BBI**<sub>2</sub><sup>2+</sup> with

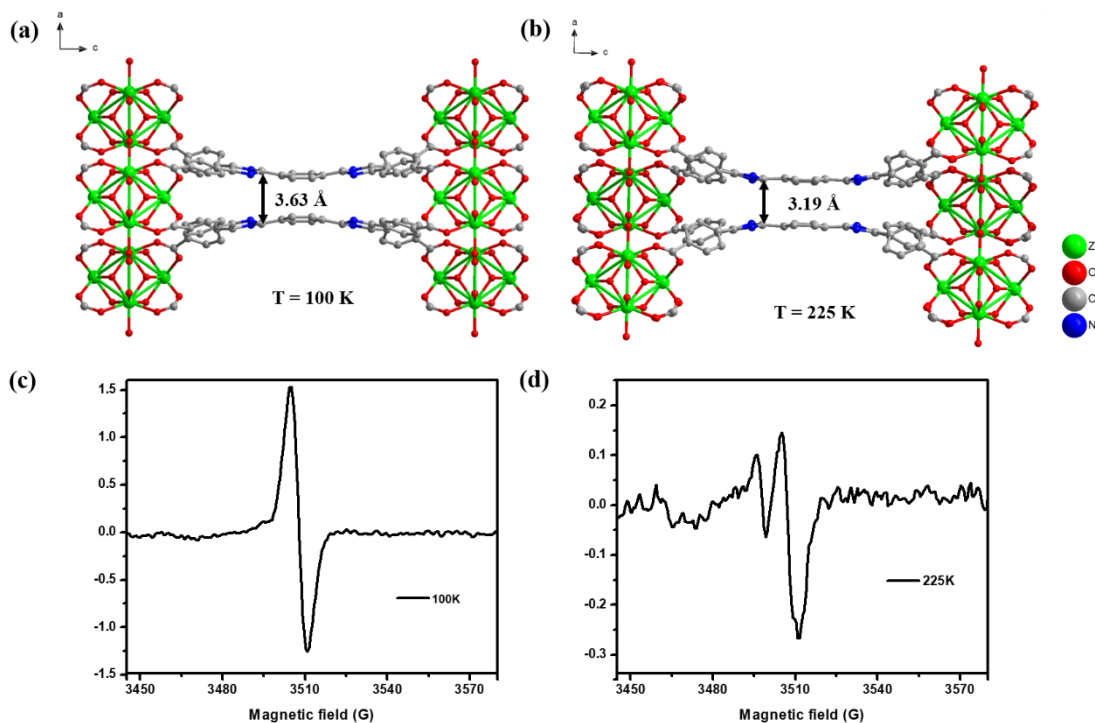


**Figure 6.** Interlinker distances of **NU-910**-acetone after irradiation at (a) 100 K, and (b) 225 K. EPR of **NU-910**-acetone in air at (c) 100 K, and (d) 225 K.

closed-shell singlet multiplicity best reproduced the experimental results of the UV-vis-NIR spectra, where the optimized geometry gave a  $\pi$ -stacking distance of 3.235 Å, while alternative charge and spin states gave null results (see the Supporting Information, p. S12-15). The calculated spectra are shown in Figure 5, where the wavelength of maximum absorption for neutral **BBI** is centered at 412 nm. Interestingly, **BBI**<sub>2</sub><sup>2+</sup> gave three prominent transitions with high oscillator strength, at 400 nm, 839 nm, and 933 nm, indicating that both low and high energy absorption bands observed experimentally can be attributed to charged states. The important transitions were visualized using charge-difference densities (CDDs) in Figure 5b, which shows how charge moves from blue to yellow orbitals upon photoexcitation. While the charge-neutral monomer displays a delocalized  $\pi$ - $\pi^*$  transition, the dicationic dimer shows clear charge-transfer (CT) behavior for lower energy (839 nm and 933 nm) excitations from the methyl benzoate tails to the  $\pi$ -dimer core where the positive charge is localized. The appearance of two distinct CT transitions arises from the “X”-shaped geometry of **BBI**, in which delocalized  $\pi$  molecular orbitals (MOs) appear as near-degenerate pairs corresponding to each long-axis diagonal element of the linker. As a dimer, degeneracy of these MOs is further removed by torsional distortions, and the electronic structure of the individual **BBI** units combine to form distinct bonding and anti-bonding MOs between linkers. Here, the transition at 933 nm transfers charge to a bonding MO and the transition at 839 nm transfers charge to an anti-bonding MO. These CT transitions are assigned to the 890 nm and 660 nm excited states, respectively, as shown in Figure 4d.

One explanation for the lower calculated excitation energy compared to experiment (e.g. 1.48 eV to 1.88 eV) was the use of an implicit solvent model that shifted CT states for charged species to lower energy, and the hybrid exchange-correlation functional, B3LYP,<sup>62-64</sup> which underestimates charge-transfer energies. Whereas the use of a long-range corrected functional ( $\omega$ B97-XD)<sup>65</sup> found that the 839 nm and 933 nm transitions were shifted to 609 nm and 855 nm, respectively, the higher energy delocalized states around 400 nm were poorly described by these methods, giving overestimations in excitation energy by > 1.0 eV and are not shown here (Figure S11).

Calculations on an isolated **BBI**<sup>•+</sup> monomer (Figure S12) found only a single optically excited state at 1105 nm that corresponds to the 643 nm absorption band in Figure 4c, with similarly underestimated excitation energy compared to experiment due to CT character. These results indicate that the radical species of **BBI** linker is more likely in a **BBI**<sup>•+</sup> cationic radical form, which converts to singlet multiplicity upon dimerization with an interaction energy<sup>66, 67</sup> of -38.2 kcal/mol; large enough to play a role in the driving force for structural contraction.<sup>68</sup> Although, this value is estimated with a small basis-set (Def2-SVP) approximation, the interaction energy is large enough that basis set error should not play a significant role. Moreover, the basis used is the same as for the excitation spectra calculations. The EPR spectrum of **NU910**-acetone-i under vacuum (Figure S9a) only shows signal contributed from the organic radical at  $g = 2.000$ , with no signal from superoxide on the Zr<sub>6</sub> node. This result indicates that the superoxide species is from the reduction of O<sub>2</sub> while excited electrons from the neutral **BBI** linker and **BBI**<sup>•+</sup> radical are generated on the MOF skeleton.

**Modulation of Radical Spin States.** To directly observe the modulation of an isolated radical and a  $\pi$ -dimer through structural tunability, we also inspected the structural changes of **NU-910** after 20 min of irradiation with a 390 nm UV lamp. For the crystal from DEF solvent after irradiation, **NU-910-DEF-i**, a symmetry breaking is observed at 100 K (Figure 3c). The space group changes from  $Cmmm$  to  $Pbam$  with very slight changes of the unit cell dimensions ( $a= 16.1453(14)$  Å,  $b= 25.6626(11)$  Å,  $c= 24.5222(7)$  Å). The site symmetry of the **BBI** linker decreases from  $C_{2h}$  to  $C_s$  and is accompanied with a static disorder at two distinct positions. On the other hand, the site symmetry of the  $Zr_6$  cluster is reduced from  $D_{2h}$  to  $C_{2h}$  due to the loss of a mirror plane perpendicular to the  $b$  axis and breaks in the C-centered translation symmetry. The C–C bond distances between phenyl ring and imidazole rings also change from 1.467(8) Å to 1.49(3) Å/1.45(2) Å, which potentially implies the changes of bond orders due to the generation of the **BBI** radical.<sup>69-71</sup> The longer C–C bond distances suggest a higher percentage of single-bond character and induce higher flexibility of the **BBI** linker after irradiation. Thus, the symmetry breaking of **NU-910-DEF-i** can be presumably attributed to the flexibility-induced relaxation of the internal stress which causes lattice deformation.<sup>64</sup> Negligible interlinker distance changes are found for the **NU-910-DEF** crystal before and after irradiation. Furthermore, the crystal structure from acetone after UV irradiation, **NU-910-acetone-i**, is also resolved at 100 K. A further contraction of the unit cell in the  $a$  direction and elongation in the  $b$  direction ( $a= 11.060(3)$  Å,  $b= 27.6231(18)$  Å,  $c= 24.2374(17)$  Å) is observed (Figure 3d). A slight increase of the C–C bond distance between the phenyl ring and imidazole rings from 1.43(2) Å to 1.46(3) Å is observed in the irradiated sample. The interlinker distance between adjacent **BBI** linkers increases from 3.20 Å to 3.63 Å (Figure 6a), which can be accounted for the internal stress-induced lattice deformation similar to the **NU-910-DEF-i** case. Moreover, as the temperature increased from 100 K to 225 K to overcome the internal lattice stress, a shorter interlinker distance of the irradiated sample is observed as 3.19 Å with longer C–C bonds (1.49(4) Å) (Figure 6b). This short interlinker distance implies a strong intermolecular interaction between adjacent radical linkers.<sup>8</sup> Furthermore, based on a new peak at 890 nm for **NU-910-acetone-i**, the formation of a radical  $\pi$ -dimer between the **BBI** linkers at 225 K is strongly suggested.

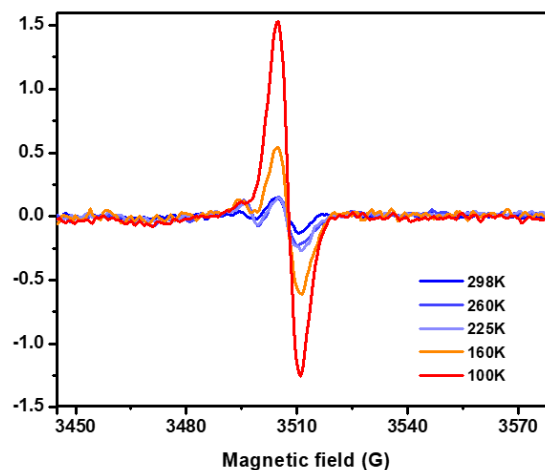


**Figure 7.** VT-EPR of **NU-910**-acetone in air.

To further confirm the formation of a  $\pi$ -dimer for the **NU-910**-acetone sample above 225 K, EPR spectra at different temperatures were collected. As shown in Figure 7, the EPR signal is mainly from superoxide radical on the  $Zr_6$  node from 298 K to 225 K. The absence of a signal from the organic radical above 225 K indicates the dimerization of radical linkers and the formation of a diamagnetic singlet state, the radical  $\pi$ -dimer. This coincides with the short interlinker distance (3.19 Å, Figure 6b) in **NU-910-acetone-i** crystal structure at 225 K. When the temperature further decreased, a strong organic radical signal at  $g = 2.000$  is observed at 160 K and becomes more intense at 100 K. The temperature dependence of the EPR signal corresponds well with the relatively long interlinker distance (3.63 Å, Figure 6a) of the **NU-910-acetone-i** crystal structure at 100 K. The EPR signals at 225 K mainly show characteristics of superoxide ions (Figure 6d) with relatively low intensity, while at 100 K, the intense signals are mostly from isolated organic radicals (Figure 6c). These spectral differences also demonstrate that organic radicals are consumed to form a radical  $\pi$ -dimer at 225 K whilst organic radicals remain isolated at 100 K. Both **NU-910-DEF** and **H<sub>4</sub>BBI** linker don't show any observable differences in EPR signals at variable temperatures (Figure S10) compared to **NU-910-acetone**, demonstrating the absence of modulation between isolated radical and radical  $\pi$ -dimer in alternative environments. In addition, EPR spectra of **NU-910-acetone** at variable temperatures under vacuum (Figure S9b) do not appreciably change compared to that of **NU-910-acetone** in air, also confirming the role of  $O_2$  in the generation of radical species from organic linkers.

## CONCLUSION

In summary, we have successfully achieved a direct observation of modulation between isolated radical and radical  $\pi$ -dimer in a flexible MOF, **NU-910**, by SCXRD and VT-EPR analysis. **NU-910** undergoes a structural contraction with the interlinker distance decreasing from 8.32 Å to 3.2 Å as the solvent exchanges from N, N-diethylformamide to acetone at 100 K. After irradiation, an increase of interlinker

distance to 3.63 Å and a strong EPR signal from an isolated radical species are observed. As the temperature increases from 100 K to 225 K, the shorter interlinker distance of 3.19 Å in the closed pore form from acetone demonstrates a strong intermolecular interaction between adjacent radical linkers while only a relatively weak signal from superoxide radical on Zr<sub>6</sub> node is detected in the EPR spectra. UV-vis-NIR and variable temperature EPR spectra in the solid state, combined with DFT calculations, confirm the formation of a radical  $\pi$ -dimer from photogenerated cation radicals in NU-910-acetone at temperatures higher than 225 K. To our knowledge, this is the first direct observation of the dynamic between isolated radical and radical  $\pi$ -dimer in a MOF system.

## EXPERIMENTAL SECTION

Experimental details can be found in the Supporting Information.

## ASSOCIATED CONTENT

The Supporting Information is available free of charge via the Internet at <http://pubs.acs.org>. Experimental and characterization data including PXRD, nitrogen isotherms, EPR spectra, <sup>1</sup>HNMR spectra, DFT calculated absorption spectra, single-crystal structures.

## AUTHOR INFORMATION

### Corresponding Author

\* Xiaofeng Chen - School of Environmental and Geographical Sciences, Shanghai Normal University, Shanghai 200234, China; [orcid.org/0000-0002-5399-9781](https://orcid.org/0000-0002-5399-9781); Email: [xiaofeng-chen@shnu.edu.cn](mailto:xiaofeng-chen@shnu.edu.cn).

\* Omar K. Farha – Department of Chemistry and International Institute of Nanotechnology, Northwestern University, Evanston, Illinois 60208, United States; Department of Chemical & Biological Engineering, Northwestern University, Evanston, Illinois 60208, United States; [orcid.org/0000-0002-9904-9845](https://orcid.org/0000-0002-9904-9845); Email: [o-farha@northwestern.edu](mailto:o-farha@northwestern.edu).

### Author Contributions

# X. C and H. X. contributed equally to this work.

### Notes

The authors declare no competing financial interest.

## ACKNOWLEDGMENT

This work was supported as part of the Inorganometallic Catalyst Design Center, an EFRC funded by the DOE, Office of Science, Basic Energy Sciences (DE-SC0012702). This work made use of the IMSERC Crystallography facility at Northwestern University, which has received support from the Soft and Hybrid Nanotechnology Experimental (SHyNE) Resource (NSF ECCS-2025633), and Northwestern University. X. C. is grateful to Prof. Kirk S. Schanze for his support, and acknowledges financial aid from the National Natural Science Foundation of China (21803038), Shanghai Municipal Education Commission, and China Scholarship Council (CSC) (202008310054) during her visit at Northwestern University. E.R.L. and Z.H.S. are supported by a National Science Foundation Graduate Research

Fellowship (DGE-1842165). We thank Dr. Zhijie Chen for critical reading and comments. We also thank Dr. Matthew Krzyaniak, Dr. Ryan Young, and Dr. Yunfan Qiu for helpful discussions. Theory calculations (CJZ and GCS), EPR spectroscopy (ERL, YQ, and MRW) and EAW were supported as part of the Center for Molecular Quantum Transduction, an Energy Frontier Research Center funded by the U.S. Department of Energy (DOE), Office of Science, Basic Energy Sciences (BES), under Award # (DE-SC0021314).

## REFERENCES

- (1) Gaita-Ariño, A.; Luis, F.; Hill, S.; Coronado, E. Molecular spins for quantum computation. *Nat. Chem.* **2019**, *11* (4), 301-309.
- (2) Kumar, K. S.; Ruben, M. Emerging trends in spin crossover (SCO) based functional materials and devices. *Coord. Chem. Rev.* **2017**, *346*, 176-205.
- (3) Wasielewski, M. R.; Forbes, M. D.; Frank, N. L.; Kowalski, K.; Scholes, G. D.; Yuen-Zhou, J.; Baldo, M. A.; Freedman, D. E.; Goldsmith, R. H.; Goodson, T. Exploiting chemistry and molecular systems for quantum information science. *Nat. Rev. Chem.* **2020**, *4* (9), 490-504.
- (4) Kippen, L.; Bernien, M.; Tuzcek, F.; Kuch, W. Spin-Crossover Molecules on Surfaces: From Isolated Molecules to Ultrathin Films. *Adv. Mater.* **2021**, *33*(49), 2008141-.
- (5) Bogani, L.; Wernsdorfer, W. Molecular spintronics using single-molecule magnets. In *Nanoscience and technology: a collection of reviews from nature journals, World Scientific* **2010**, 194-201.
- (6) Mas-Torrent, M.; Crivillers, N.; Mugnaini, V.; Ratera, I.; Rovira, C.; Veciana, J. Organic radicals on surfaces: towards molecular spintronics. *J. Mater. Chem.* **2009**, *19* (12), 1691-1695.
- (7) Lü, B.; Chen, Y.; Li, P.; Wang, B.; Müllen, K.; Yin, M. Stable radical anions generated from a porous peryleneimide metal-organic framework for boosting near-infrared photothermal conversion. *Nat. Commun.* **2019**, *10* (1), 1-8.
- (8) Kertesz, M. Pancake bonding: An unusual Pi-stacking interaction. *Chem. Eur. J.* **2019**, *25* (2), 400-416.
- (9) Gütllich, P.; Goodwin, H. A.; Boillot, M.-L. *Spin crossover in transition metal compounds I. Springer* **2004**, Vol. 233.
- (10) Zhao-Yang Li, O. S.; Yao, Z.-S.; Kang, S.; Kanegawa, S., Multifunctional Materials Combining Spin-Crossover with Conductivity and Magnetic Ordering. In *Spin-Crossover Materials*, 2013; pp 303-319.
- (11) Senthil Kumar, K.; Ruben, M., Emerging Trends in Spin Crossover (SCO) Based Functional Materials and Devices. *Coordination Chemistry Reviews* **2017**, *346*, 176-205.
- (12) Murray, K. S. The Development of Spin-Crossover Research. *Spin-Crossover Materials: Properties and Applications* **2013**, 1-54.
- (13) Gütllich, P.; Goodwin, H. A.; Boillot, M.-L. *Spin crossover in transition metal compounds I. Springer* **2004**, Vol. 233.
- (14) Kawamura, A.; Xie, J.; Boyn, J.-N.; Jesse, K. A.; McNeece, A. J.; Hill, E. A.; Collins, K. A.; Valdez-Moreira, J. A.; Filatov, A. S.; Kurutz, J. W. Reversible Switching of Organic Diradical Character via Iron-Based Spin-crossover. *J. Am. Chem. Soc.* **2020**, *142* (41), 17670-17680.
- (15) Geraskina, M. R.; Buck, A. T.; Winter, A. H. An Organic Spin Crossover Material in Water from a covalently linked radical dyad. *J. Org. Chem.* **2014**, *79* (16), 7723-7727.
- (16) Buck, A. T.; Paletta, J. T.; Khindurangala, S. A.; Beck, C. L.; Winter, A. H. A noncovalently reversible paramagnetic switch in water. *J. Am. Chem. Soc.* **2013**, *135* (29), 10594-10597.
- (17) Peterson, J. P.; Winter, A. H. Solvent effects on the stability and delocalization of aryl dicyanomethyl radicals: The captodative effect revisited. *J. Am. Chem. Soc.* **2019**, *141* (32), 12901-12906.
- (18) Geraskina, M. R.; Dutton, A. S.; Juetten, M. J.; Wood, S. A.; Winter, A. H. The Viologen Cation Radical Pimer: A Case of Dispersion-Driven Bonding. *Angew. Chem.* **2017**, *129* (32), 9563-9567.
- (19) Wang, Y.; Frascioni, M.; Stoddart, J. F. Introducing stable

- radicals into molecular machines. *ACS Cent. Sci.* **2017**, *3* (9), 927-935.
- (20) Peterson, J. P.; Ellern, A.; Winter, A. H. Spin delocalization, polarization, and London dispersion forces govern the formation of diradical dimers. *J. Am. Chem. Soc.* **2020**, *142* (11), 5304-5313
- (21) Itkis, M.; Chi, X.; Cordes, A.; Haddon, R. Magneto-optoelectronic bistability in a phenalenyl-based neutral radical. *Science* **2002**, *296* (5572), 1443-1445.
- (22) Koivisto, B. D.; Ichimura, A. S.; McDonald, R.; Lemaire, M. T.; Thompson, L. K.; Hicks, R. G. Intramolecular  $\pi$ -Dimerization in a 1,1'-Bis(verdazyl) ferrocene Diradical. *J. Am. Chem. Soc.* **2006**, *128* (3), 690-691.
- (23) Chen, Q.; Sun, J.; Li, P.; Hod, I.; Moghadam, P. Z.; Kean, Z. S.; Snurr, R. Q.; Hupp, J. T.; Farha, O. K.; Stoddart, J. F. A redox-active bistable molecular switch mounted inside a metal-organic framework. *J. Am. Chem. Soc.* **2016**, *138* (43), 14242-14245.
- (24) Yaghi, O. M.; O'Keeffe, M.; Ockwig, N. W.; Chae, H. K.; Eddaoudi, M.; Kim, J. Reticular synthesis and the design of new materials. *Nature* **2003**, *423* (6941), 705-714.
- (25) Zhou, H.-C.; Long, J. R.; Yaghi, O. M. Introduction to metal-organic frameworks. *Chem. Rev.* **2012**, *112* (2), 673-674.
- (26) Tanabe, K. K.; Cohen, S. M. Postsynthetic modification of metal-organic frameworks—a progress report. *Chem. Soc. Rev.* **2011**, *40* (2), 498-519.
- (27) Razavi, S. A. A.; Morsali, A. Linker functionalized metal-organic frameworks. *Coord. Chem. Rev.* **2019**, *399*, 213023.
- (28) Bernales, V.; Ortuño, M. A.; Truhlar, D. G.; Cramer, C. J.; Gagliardi, L. Computational design of functionalized metal-organic framework nodes for catalysis. *ACS Cent. Sci.* **2018**, *4* (1), 5-19.
- (29) Zhao, D.; Timmons, D. J.; Yuan, D.; Zhou, H.-C. Tuning the topology and functionality of metal-organic frameworks by ligand design. *Acc. Chem. Res.* **2011**, *44* (2), 123-133.
- (30) Stock, N.; Biswas, S. Synthesis of metal-organic frameworks (MOFs): routes to various MOF topologies, morphologies, and composites. *Chem. Rev.* **2012**, *112* (2), 933-969.
- (31) Chen, Z.; Hanna, S. L.; Redfern, L. R.; Alezi, D.; Islamoglu, T.; Farha, O. K. Reticular chemistry in the rational synthesis of functional zirconium cluster-based MOFs. *Coord. Chem. Rev.* **2019**, *386*, 32-49.
- (32) Schneemann, A.; Bon, V.; Schwedler, I.; Senkowska, I.; Kaskel, S.; Fischer, R. A. Flexible Metal-Organic Frameworks. *Chem. Soc. Rev.* **2014**, *43* (16), 6062-6096.
- (33) Pallach, R.; Keupp, J.; Terlinden, K.; Frenzel-Beyme, L.; Kloß, M.; Machalica, A.; Kotschy, J.; Vasa, S. K.; Chater, P. A.; Sternemann, C.; Wharmby, M. T.; Linser, R.; Schmid, R.; Henke, S. Frustrated Flexibility in Metal-Organic Frameworks. *Nat. Commun.* **2021**, *12* (1), 4097.
- (34) Kaur, J.; Kaur, G. Review on Flexible Metal-Organic Frameworks. *ChemistrySelect* **2021**, *6* (32), 8227-8243.
- (35) Kitagawa, S.; Uemura, K. Dynamic Porous Properties of Coordination Polymers Inspired by Hydrogen Bonds. *Chem. Soc. Rev.* **2005**, *34* (2), 109-119.
- (36) Férey, G.; Serre, C. Large breathing effects in three-dimensional porous hybrid matter: facts, analyses, rules and consequences. *Chem. Soc. Rev.* **2009**, *38* (5), 1380-1399.
- (37) Howarth, A. J.; Liu, Y.; Li, P.; Li, Z.; Wang, T. C.; Hupp, J. T.; Farha, O. K. Chemical, thermal and mechanical stabilities of metal-organic frameworks. *Nat. Rev. Mater.* **2016**, *1* (3), 1-15.
- (38) Bai, Y.; Dou, Y.; Xie, L.-H.; Rutledge, W.; Li, J.-R.; Zhou, H.-C. Zr-based metal-organic frameworks: design, synthesis, structure, and applications. *Chem. Soc. Rev.* **2016**, *45* (8), 2327-2367.
- (39) Li, Z.; Peters, A. W.; Bernales, V.; Ortuño, M. A.; Schweitzer, N. M.; DeStefano, M. R.; Gallington, L. C.; Platero-Prats, A. E.; Chapman, K. W.; Cramer, C. J. Metal-organic framework supported cobalt catalysts for the oxidative dehydrogenation of propane at low temperature. *ACS Cent. Sci.* **2017**, *3* (1), 31-38.
- (40) Zhang, X.; Frey, B. L.; Chen, Y.-S.; Zhang, J. Topology-guided stepwise insertion of three secondary linkers in zirconium metal-organic frameworks. *J. Am. Chem. Soc.* **2018**, *140* (24), 7710-7715.
- (41) Deria, P.; Gómez-Gualdrón, D. A.; Bury, W.; Schaefer, H. T.; Wang, T. C.; Thallapally, P. K.; Sarjeant, A. A.; Snurr, R. Q.; Hupp, J. T.; Farha, O. K. Ultraporos, water stable, and breathing zirconium-based metal-organic frameworks with ftw topology. *J. Am. Chem. Soc.* **2015**, *137* (40), 13183-13190.
- (42) Chen, C. X.; Yin, S. Y.; Wei, Z. W.; Qiu, Q. F.; Zhu, N. X.; Fan, Y. N.; Pan, M.; Su, C. Y. Pressure-Induced Multiphoton Excited Fluorochromic Metal-Organic Frameworks for Improving MPEF Properties. *Angew. Chem.* **2019**, *131* (40), 14517-14523
- (43) Islamoglu, T.; Otake, K.-i.; Li, P.; Buru, C. T.; Peters, A. W.; Akpınar, I.; Garibay, S. J.; Farha, O. K. Revisiting the structural homogeneity of NU-1000, a Zr-based metal-organic framework. *CrystEngComm* **2018**, *20* (39), 5913-5918.
- (44) Mihalcik, D. J.; Zhang, T.; Ma, L.; Lin, W. Highly porous 4, 8-connected metal-organic frameworks: synthesis, characterization, and hydrogen uptake. *Inorg. Chem.* **2012**, *51* (4), 2503-2508.
- (45) Lv, X.-L.; Xie, L.-H.; Wang, B.; Zhao, M.; Cui, Y.; Li, J.-R. Flexible metal-organic frameworks for the wavelength-based luminescence sensing of aqueous pH. *J. Mater. Chem. C* **2018**, *6* (39), 10628-10639.
- (46) Li, L.; Tu, Z.-M.; Hua, Y.; Li, X.-N.; Wang, H.-Y.; Zhang, H. A novel multifunction photochromic metal-organic framework for rapid ultraviolet light detection, amine-selective sensing and inkless and erasable prints. *Inorg. Chem. Front.* **2019**, *6* (11), 3077-3082.
- (47) Sun, J.-K.; Cai, L.-X.; Chen, Y.-J.; Li, Z.-H.; Zhang, J. Reversible luminescence switch in a photochromic metal-organic framework. *Commun. Chem.* **2011**, *47* (24), 6870-6872.
- (48) Liu, J.-J.; Que, Q.-T.; Liu, D.; Suo, H.; Liu, J.; Xia, S.-B. A multifunctional photochromic metal-organic framework with Lewis acid sites for selective amine and anion sensing. *CrystEngComm* **2020**, *22* (24), 4124-4129.
- (49) Han, L.; Qin, L.; Xu, L.; Zhou, Y.; Sun, J.; Zou, X. A novel photochromic calcium-based metal-organic framework derived from a naphthalene diimide chromophore. *Commun. Chem.* **2013**, *49* (4), 406-408.
- (50) Mallick, A.; Garai, B.; Addicoat, M. A.; Petkov, P. S.; Heine, T.; Banerjee, R. Solid state organic amine detection in a photochromic porous metal organic framework. *Chem. Sci.* **2015**, *6* (2), 1420-1425.
- (51) Zhou, Y.; Qin, L.; Wu, M.-K.; Han, L. A bifunctional anionic metal-organic framework: reversible photochromism and selective adsorption of methylene Blue. *Cryst. Growth Des.* **2018**, *18* (10), 5738-5744.
- (52) Sherman, D. A.; Murase, R.; Duyker, S. G.; Gu, Q.; Lewis, W.; Lu, T.; Liu, Y.; D'Alessandro, D. M. Reversible single crystal-to-single crystal double [2+2] cycloaddition induces multifunctional photo-mechano-electrochemical properties in framework materials. *Nat. Commun.* **2020**, *11* (1), 1-10
- (53) Narayan, T. C.; Miyakai, T.; Seki, S.; Dincă, M. High charge mobility in a tetrathiafulvalene-based microporous metal-organic framework. *J. Am. Chem. Soc.* **2012**, *134* (31), 12932-12935.
- (54) Su, J.; Yuan, S.; Wang, H.-Y.; Huang, L.; Ge, J.-Y.; Joseph, E.; Qin, J.; Cagin, T.; Zuo, J.-L.; Zhou, H.-C. Redox-switchable breathing behavior in tetrathiafulvalene-based metal-organic frameworks. *Nat. Commun.* **2017**, *8* (1), 1-8.
- (55) Jindal, S.; Maka, V. K.; Moorthy, J. N. Selective sensing of aliphatic biogenic polyamines by a zwitterionic Cd-MOF based on bisimidazole tetracarboxylic acid linker. *J. Mater. Chem. C* **2020**, *8* (33), 11449-11456.
- (56) Yamaguchi, T.; Hatano, S.; Abe, J. Multistate photochromism of 1-phenyl-naphthalene-bridged imidazole dimer that has three colorless isomers and two colored isomers. *J. Phys. Chem. A* **2014**, *118* (1), 134-143.
- (57) Ito, H.; Tanaka, S.; Mutoh, K.; Abe, J. Fast Photochromism of the Imidazole Dimers Bridged by Group 14 Atoms. *Org. Lett.* **2020**, *22*

- (14), 5680-5684.
- (58) Kometani, A.; Inagaki, Y.; Mutoh, K.; Abe, J. Red or Near-Infrared Light Operating Negative Photochromism of a Binaphthyl-Bridged Imidazole Dimer. *J. Am. Chem. Soc.* **2020**, *142* (17), 7995-8005.
- (59) Gionco, C.; Paganini, M. C.; Giamello, E.; Burgess, R.; Di Valentin, C.; Pacchioni, G. Paramagnetic defects in polycrystalline zirconia: an EPR and DFT study. *Chem. Mater.* **2013**, *25* (11), 2243-2253.
- (60) Ji, P.; Feng, X.; Oliveres, P.; Li, Z.; Murakami, A.; Wang, C.; Lin, W. Strongly Lewis acidic metal-organic frameworks for continuous flow catalysis. *J. Am. Chem. Soc.* **2019**, *141* (37), 14878-14888.
- (61) Nishinaga, T.; Sotome, Y. Stable Radical Cations and Their  $\pi$ -Dimers Prepared from Ethylene- and Propylene-3,4-dioxythiophene Co-oligomers: Combined Experimental and Theoretical Investigations. *J. Org. Chem.* **2017**, *82* (14), 7245-7253.
- (62) Becke, A. D. Density-functional exchange-energy approximation with correct asymptotic behavior. *Phys. Rev. A* **1988**, *38* (6), 3098.
- (63) Beck, A. D. Density-functional thermochemistry. III. The role of exact exchange. *J. Chem. Phys.* **1993**, *98* (7), 5648-6.
- (64) Lee, C.; Yang, W.; Parr, R. G. Development of the Colle-Salvetti correlation-energy formula into a functional of the electron density. *Phys. Rev. B* **1988**, *37* (2), 785.
- (65) Chai, J.-D.; Head-Gordon, M. Long-range corrected hybrid density functionals with damped atom-atom dispersion corrections. *Phys. Chem. Chem. Phys.* **2008**, *10* (44), 6615-6620.
- (66) Kertesz, M. Pancake bonding: An unusual  $\pi$ -stacking interaction. *Chem. Eur. J.* **2019**, *25* (2), 400-416.
- (67) Mou, Z.; Kubo, T.; Kertesz, M. Hetero- $\pi$ -Dimers of Phenalenyls. *Chem. Eur. J.* **2015**, *21* (50), 18230-18236.
- (68) Cai, K.; Zhang, L.; Astumian, R. D.; Stoddart, J. F. Radical-pairing-induced molecular assembly and motion. *Nat. Rev. Chem.* **2021**, 1-19.
- (69) Rottschäfer, D.; Ho, N. K. T.; Neumann, B.; Stämmler, H. G.; van Gastel, M.; Andrada, D. M.; Ghadwal, R. S. N-Heterocyclic Carbene Analogues of Thiele and Chichibabin Hydrocarbons. *Angew. Chem.* **2018**, *130* (20), 5940-5944.
- (70) Kishimoto, Y.; Abe, J. A fast photochromic molecule that colors only under UV light. *J. Am. Chem. Soc.* **2009**, *131* (12), 4227-4229.
- (71) Wieme, J.; Lejaeghere, K.; Kresse, G.; Van Speybroeck, V. Tuning the balance between dispersion and entropy to design temperature-responsive flexible metal-organic frameworks. *Nat. Commun.* **2018**, *9* (1), 1-10.

